

Leveraging Semantic Asymmetry for Precise Gross Tumor Volume Segmentation of Nasopharyngeal Carcinoma in Planning CT

Zi Li^{*1,4}, Ying Chen³, Zeli Chen^{1,4}, Yanzhou Su^{1,4}, Tai Ma^{1,2},
Tony C. W. Mok^{1,4}, Yan-Jie Zhou^{1,4}, Yunhao Bai^{1,2}, Zhinlin Zheng^{1,4}, Le Lu¹,
Yirui Wang¹, Jia Ge³, Xianghua Ye³, Senxiang Yan³, and Dakai Jin¹

¹ DAMO Academy, Alibaba Group

² East China Normal University, Shanghai, China

³ The First Affiliated Hospital of College of Medicine, Zhejiang University, China

⁴ Hupan Lab, Hangzhou, China

alisonbrielee@gmail.com

Abstract. In the radiation therapy of nasopharyngeal carcinoma (NPC), clinicians typically delineate the gross tumor volume (GTV) using non-contrast planning computed tomography to ensure accurate radiation dose delivery. However, the low contrast between tumors and adjacent normal tissues requires radiation oncologists to manually delineate the tumors with additional reference from MRI images. In this study, we propose a novel approach to directly segment NPC gross tumors on non-contrast planning CT images, circumventing potential registration errors when aligning MRI or MRI-derived tumor masks to planning CT. To address the low contrast issues between tumors and adjacent normal structures in planning CT, we introduce a 3D Semantic Asymmetry Tumor Segmentation (SATS) method. Specifically, we posit that a healthy nasopharyngeal region is characteristically bilaterally symmetric, whereas the presence of nasopharyngeal carcinoma disrupts this symmetry. Then, we propose a Siamese contrastive learning segmentation framework that minimizes the voxel-wise distance between original and flipped areas without tumor and encourages a larger distance between original and flipped areas with tumor. Thus, our approach enhances the sensitivity of deep features to semantic asymmetries. Extensive experiments demonstrate that the proposed SATS achieves the leading NPC GTV segmentation performance in both internal and external testing, *e.g.*, with at least 2% absolute Dice score improvement and 12% average surface distance error reduction when compared to other state-of-the-art methods in the external testing.

Keywords: Nasopharyngeal Carcinoma · Gross Tumor Volume · Asymmetry-inspired Segmentation · Deep learning · Radiation Therapy.

* Corresponding author.

1 Introduction

Nasopharyngeal carcinoma (NPC) ranks among the most prevalent head & neck malignancies affecting the nasopharyngeal region, with patient prognosis substantially enhanced through early diagnosis and intervention [8]. A significant proportion of NPC patients can achieve complete remission following radiation therapy (RT) [7]. Notably, this type of cancer exhibits a remarkable sensitivity to radiation therapy, wherein a pivotal component of this therapeutic intervention is the accurate delineation of the gross tumor volume (GTV). In clinical practice, magnetic resonance imaging (MRI) has emerged as the predominant imaging modality for NPC, owing to its superior resolution in visualizing soft tissues. Subsequently, cross-modality registration is conducted between MRI and non-contrast planning computed tomography (pCT) to transfer tumor delineations from MRI to pCT scans for the treatment planning [33]. However, cross-modality registration is non-trivial due to substantial modality gaps and variations in scanning ranges. Alternatively, physicians may integrate pCT and MRI mentally to assist in delineating the GTV. Nevertheless, this approach is time-consuming, often taking 1-2 hours per case, and is prone to potential inaccuracies.

Recently, learning-based approaches have yielded promising outcomes in NPC tumor segmentation from MRI scans [13, 17, 20–22, 27, 28]. Nonetheless, this modality fails to provide direct measurements of electron density essential for radiotherapy planning. MRI-derived tumor masks necessitate spatial transformation to pCT via image registration, which often introduces alignment errors. Some approaches [5, 30] propose to tackle the automated NPC GTV segmentation using both CT and MRI. Notably, registration errors between paired CT and MRI can lead to inferior multi-modality segmentation performance as compared to single-modality methods. Additionally, researches [2, 19, 31, 32] have focused on segmenting the NPC GTV using contrast-enhanced CT scans. However, these approaches yield relatively low performance, *e.g.*, Dice score falling below 70%. This limitation is attributed to the invasive capability of NPC tumors into adjacent tissues and the suboptimal contrast of pCT, especially regarding soft tissues like mucous membranes, muscles, and nerves.

In this work, our goal is to segment NPC GTV in non-contrast pCT, which could avoid registration errors when aligning MRI or MRI-derived tumor masks to pCT. Directly segmenting NPC GTV in non-contrast pCT is challenging because the boundaries between the NPC tumor and adjacent soft tissues, such as membranes, muscles, and vessels, are extremely unclear in non-contrast pCT. To alleviate this issue, we propose a 3D Semantic Asymmetry Tumor Segmentation (SATS) method based on the observation that a healthy nasopharyngeal region is typically bilaterally symmetric, but the presence of an NPC tumor disrupts this symmetry, as illustrated in Figure 1. Specifically, to exploit the anatomical symmetry cue, we first wrap the pCT using automatically segmented head and neck landmark organs so that the pCT is bilaterally symmetric along the central sagittal plane. This helps to reduce the influence of asymmetric anatomies caused by patient’s head location and pose variation during the CT scanning. Then, we develop a Siamese contrastive learning segmentation framework based

on conventional segmentation loss and an additional voxel-level margin loss. The margin loss is applied to deep features extracted from the original pCT and flipped pCT scan, which aims to minimize the voxel-wise distance between original and flipped areas without tumor, and encourage larger distance between original and flipped areas with tumor, making GTV features more sensitive to semantic asymmetries. To determine the asymmetrical nasopharyngeal areas, we present a tumor mask-based region selection approach.

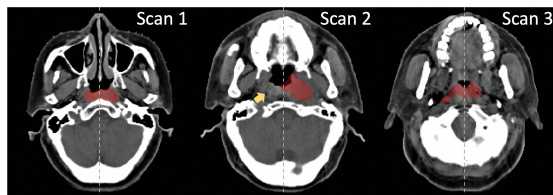


Fig. 1: Example head CT images illustrate that the area of the gross tumor is mostly asymmetrical and how anatomical symmetry aids in distinguishing abnormalities. The lesions become more discernible when comparing anatomically symmetric regions.

The main contributions of this work are as follows:

- We introduce a 3D *semantic asymmetry tumor segmentation (SATS)* method for NPC GTV in non-contrast pCT, which is the most common imaging modality in RT planning. To the best of our knowledge, this is the first work to tackle the NPC GTV segmentation in non-contrast CT scans and employ the symmetry cue for the GTV segmentation.
- We develop a Siamese contrastive learning segmentation framework with an asymmetrical region selection approach, which facilitates the learning of asymmetric tumor features effectively.
- We demonstrate that our proposed SATS achieves *state-of-the-art* performance in NPC GTV segmentation, outperforming the leading methods in both internal and independent external testing datasets.

2 Related Work

2.1 Learning-based GTV Segmentation in NPC

Recently, learning-based approaches have made great progress in NPC GTV segmentation. The work in [26, 32] applies deep networks to segment tumors in contrast-enhanced CT. Chen *et al.* targets the segmentation of tumors by integrating cross-modality features of MRI and CT [5]. NPCNet [20] is designed to segment both primary tumors and metastatic lymph nodes in 2D MRI slices. Researchers [36] investigate domain adaptation techniques and utilize limited

annotated target data to enhance the performance of GTV segmentation in MRI.

Current approaches predominantly rely on MRI and/or contrast-enhanced CT for NPC GTV segmentation, as it has long been believed that identifying NPC GTV in non-contrast CT is an extremely challenging (if not impossible) task. To date, effective segmentation methods on non-contrast pCT remain elusive. However, pCT is mostly adopted in RT routine without contrast injection, and transforming MRI-derived tumor masks to pCT inevitably involves considerable alignment errors. In this work, we directly segment NPC GTV in non-contrast pCT by leveraging the tumor-induced asymmetry.

2.2 Symmetry in Medical Image Analysis

Human anatomy usually displays bilateral symmetry, as observed in structures such as the brain, breasts, lungs, and pelvis. Leveraging this symmetry has been crucial in various medical image analysis tasks. As for the brain, asymmetry in the shape of subcortical structures has been linked to Alzheimer’s disease, and researchers [23] have applied the shape analysis technique along with machine learning to quantify these asymmetries. Similarly, a siamese Faster R-CNN approach [24] has been proposed for breast cancer detection, which performs joint analysis of both breasts to detect masses in mammographic images and utilizes inherent bilateral symmetry to improve detection performance. In addition, researchers [4] have explored semantic asymmetry for accurate Pelvic fracture detection in X-ray images. These applications [4, 14, 23, 24] underscore the utility of symmetry-based approaches in medical image analysis, *i.e.*, offering improved diagnostic accuracy and early detection capabilities by leveraging the symmetrical nature of anatomical structures.

3 Method

We propose a 3D semantic asymmetry tumor segmentation (SATS) method based on the semantic asymmetry property of the gross tumor in the nasopharyngeal area, to enable accurate NPC GTV segmentation. Given one CT scan, as shown in Figure 2 (a), we utilize a shared encoder-decoder module to process both the original image $I \in \mathbb{R}^{D \times H \times W}$, where D, H, W are CT image spatial dimensions, and its flipped image I' , thereby encoding them into a symmetric representation. Subsequently, we introduce a non-linear projection module and a distance metric learning strategy to refine the resulting feature maps. We intend to maximize the dissimilarity between E and E_f at corresponding anatomical locations on the abnormalities and normalities. The distance metric learning paradigm is illustrated in Figure 2 (b).

3.1 Asymmetrical Abnormal Region Selection

The focus of our SATS model is to pay attention to the asymmetric abnormal area. We design a supervised ROI-selection method to detect asymmetric

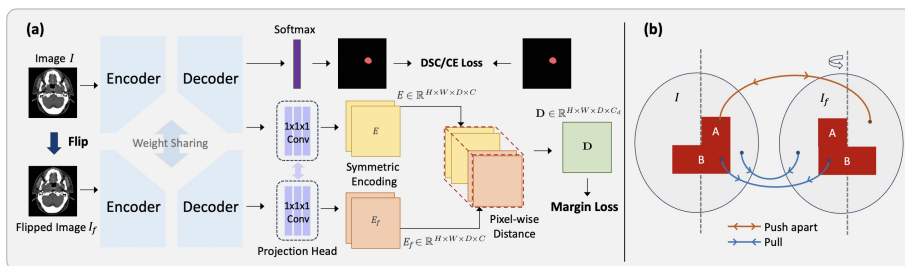


Fig. 2: **(a)** Our SATS model begins with the encoder-decoder module, which uses shared weights to process two input signals and encode them into a discriminative representation. This representation is then further processed through a non-linear projection module and a distance metric learning module to produce feature maps. **(b)** A graphical representation of our metric learning strategy. Circles indicate individual CT images, I , while red squares highlight the tumors. The tumors are composed of A and B, representing symmetrical and asymmetrical lesions relative to the central sagittal axis of symmetry, respectively.

abnormal areas using the available tumor annotation. Considering that image asymmetry may originate from pathological or non-pathological sources, such as changes in imaging angles and patient postures, we pre-process the CT scans using [35] to ensure that the scans are *symmetric along the central sagittal axis*. Specifically, we manually select a patient CT image with bilateral symmetry along the central sagittal plane, which serves as an atlas, and then align other patient CT images to the atlas space through affine registration. This step helps to alleviate the influence of other asymmetrical anatomical structures in head & neck that may mislead the model.

The semantic segmentation mask of I is denoted as $s \in \{0, 1\}^{D \times H \times W}$, where 0 represents the background and 1 represents the foreground of tumors. Through the flip operation, we can obtain the flipped semantic mask s' of I' . Subsequently, an asymmetrical mask \mathbf{m} is defined to locate asymmetrical regions in the image I , as

$$\mathbf{m} = s - s \cap s' \quad (1)$$

where $\mathbf{m} \in \{0, 1\}^{D \times H \times W}$. Note that 1 and 0 represent the asymmetrical and symmetrical regions in I , respectively.

3.2 Asymmetrical Learning Strategy

Our segmentation loss function is comprised of two components: a combination of Dice and entropy loss for the conventional segmentation purpose, and a voxel-wise margin loss specifically designed for asymmetric abnormal regions.

Metric-based margin loss. In the asymmetric anomaly region, we aim to minimize the similarity between the features of any point and its corresponding point on the central sagittal axis. To achieve this, we employ pixel-level margin loss. Based on above asymmetrical abnormal region \mathbf{m} , the margin loss between features $E \in \mathbb{R}^{H \times W \times D \times C}$, where C is the number of output features, and flipped E' after a non-linear projection is as:

$$l_{margin} = \sum_{i,j,k}^{D,H,W} [\mathbf{1}_{(m(i,j,k)=1)} \|E(i,j,k) - E'(i,j,k)\|^2 + \mathbf{1}_{(m(i,j,k) \neq 1)} \max(t - \|E(i,j,k) - E'(i,j,k)\|^2, 0)] \quad (2)$$

where $\mathbf{1}$ is the indicator function, and t defines a margin that regulates the degree of dissimilarity in semantic asymmetries.

Overall loss function. We approach tumor segmentation as a binary segmentation task, utilizing the Dice loss, binary cross-entropy loss, and margin loss as our objective function. The overall loss function is formulated as follows:

$$l = l_{dice} + l_{ce} + \beta l_{margin}, \quad (3)$$

where β is the weight balancing the different losses.

3.3 Siamese Segmentation Architecture

Our SATS architecture comprises the encoder-decoder module and the projection head. While both components are engaged during the training process, only the encoder-decoder module is required during inference.

Siamese encoder-decoder. The backbone is a shared U-shaped encoder-decoder architecture, as shown in Fig. 2. The encoder employs repeated applications of 3D residual blocks, with each block comprising two convolutional layers with $3 \times 3 \times 3$ kernels. Each convolutional layer is succeeded by InstanceNorm normalization and LeakyReLU activation. For downsampling, a convolutional operation with a stride of 2 is utilized to halve the resolution of the input feature maps. The initial number of filters is 32 and doubles after each downsampling step to maintain constant time complexity except for the last layer. In total, the encoder performs four downsampling operations.

Projection head. We utilize a non-linear projection g to transform the features before calculating the distance in margin loss, which aims to enhance the quality of the learned features. It consists of three $1 \times 1 \times 1$ convolution layers with 16 channels followed by a unit-normalization layer. The first two layers in the projection head use the ReLU activation function. We hypothesize that directly applying metric learning to segmentation features might lead to information loss and diminish the model’s effectiveness. For example, some asymmetries in CT images are non-pathological and may stem from variations in the patient’s

head positioning and posing, yet they are beneficial for segmentation. Utilizing a non-linear projection may filter out such irrelevant information from the metric learning process, ensuring it is preserved in the features used for segmentation.

4 Experiments

4.1 Data Preparation

We collected and curated an *in-house dataset* from our internal hospital for the model development, which consisted of 163 NPC patients with pCT, contrast-enhanced diagnostic CT, and diagnostic MRIs of T1 & T2 phases. Diagnostic CT and MRI were registered as, initially, a rigid transformation [1] was applied to the MRI images to approximately align with the CT images, ensuring a similar anatomical positioning. Subsequently, the cross-modality deformable registration algorithm, deeds [12], was utilized to achieve precise local appearance alignment. The contrast-enhanced CT and MRIs are used to guide radiation oncologists to generate ground-truth GTV in pCT.

Additionally, we collected and curated a public dataset, SegRap2023⁵, as *external testing dataset*, containing 118 no-contrast pCT and enhanced CT. We observe that original tumor annotations in SegRap2023 are generally larger than the NPC GTV guideline’s description [18]. Hence, we curated their labels. *Annotations of all datasets were examined and edited by two experienced radiation oncologists following the international GTV delineation consensus guideline [18].* For evaluation, 20 % of the in-house dataset was randomly selected as the internal testing set, and the entire curated SegRap2023 was used as the external testing dataset. As illustrated in Figure 3, the asymmetric regions in the external data are larger than those in the in-house data, making the task more challenging.

⁵ <https://segrap2023.grand-challenge.org/dataset/>

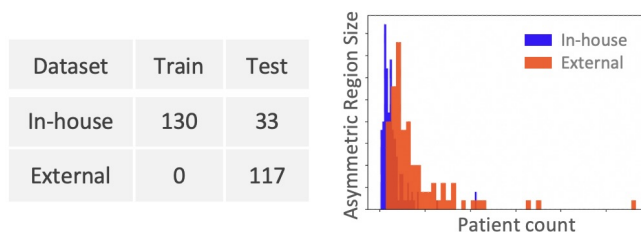


Fig. 3: Left: the data partitioning situation of the main comparing experiment. Right: the size of the asymmetric regions of different individuals on the two datasets, with the x-axis displaying each test object.

Table 1: Quantitative results on NPC GTV segmentation task. The experiment is denoted as $\text{In-house}_{train} \Rightarrow \text{In-house}_{test}$, which represents training on scans from the In-house dataset and segmenting images in the test set of the In-house dataset. \uparrow : Higher values are better. \downarrow : Lower values are better. The last column presents the number of model parameters (in millions) of various segmentation methods. The best-performing results are shown in bold while the second-best results are indicated by underlining.

Method	In-house _{train} \Rightarrow In-house _{test}			Para. Count (M)
	DSC \uparrow	ASD \downarrow	HD95 \downarrow	
UMambaBot	79.27 \pm 7.77	1.17 \pm 0.77	4.66 \pm 3.93	64.76
UNETR	75.75 \pm 8.92	1.32 \pm 0.70	5.41 \pm 4.07	93.01
TransUNet	78.95 \pm 8.28	1.58 \pm 2.53	6.42 \pm 12.89	119.37
SwinUNETR	80.01 \pm 8.04	1.19 \pm 0.72	4.52 \pm 2.77	62.19
SwinUNETR-v2	<u>80.41 \pm 7.80</u>	1.17 \pm 0.68	4.17 \pm 2.40	72.89
MedNeXt	76.15 \pm 9.83	1.44 \pm 0.88	5.09 \pm 3.93	61.80
STU-Net S	79.04 \pm 7.30	1.18 \pm 0.74	4.95 \pm 4.08	14.60
STU-Net B	78.86 \pm 7.38	1.20 \pm 0.73	4.91 \pm 3.98	58.26
STU-Net L	79.24 \pm 7.23	1.19 \pm 0.72	4.64 \pm 3.80	440.30
nnUNet	79.30 \pm 9.77	<u>1.16 \pm 0.84</u>	<u>4.07 \pm 2.77</u>	30.70
SATS (Ours)	81.22 \pm 8.33	1.14 \pm 0.84	4.02 \pm 2.74	30.70

4.2 Implementation

During training, we employed the stochastic gradient descent algorithm [3] with a momentum of 0.99 as the optimizer. The model training is divided into two stages. In the first stage, only the Siamese encoder-decoder is trained for 800 epochs with a learning rate of $1e-2$ and decayed via a polynomial schedule. In the second stage, the projection head is trained for 200 epochs, with a learning rate of $1e-2$ for the projection head and $1e-5$ for the Siamese encoder-decoder, both with decayed via a polynomial schedule. The patch size is $56 \times 192 \times 192$ and the batch size is 2. For the voxel-wise contrastive loss, we use a margin hyperparameter $t = 20$ and $\beta = 1$.

4.3 Comparison Methods and Evaluation Metrics

We conducted a comprehensive comparison of our method with **ten** cutting-edge approaches, encompassing prominent CNN-based, Transformer-based and Mamba-based methods, to evaluate its performance. CNN-based methods include STU-Net S [15], STU-Net B [15], STU-Net L [15], MedNeXt [34] and nnUNet [16]. Transformer-based methods include UNETR [10], TransUNet [6], SwinUNETR [9] and its variant SwinUNETR-v2 [11]. Mamba-based methods include UMambaBot [29].

To maintain a fair comparison, we trained all competing models for an equal number of epochs, 1000. We use different learning rates for different comparative methods to avoid model collapse during training. Typically, CNN-based methods

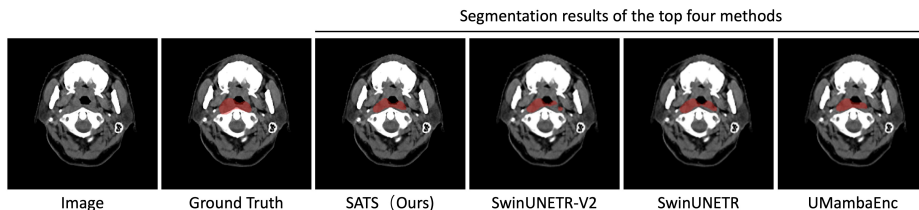


Fig. 4: Example CT slices with tumor segmentation overlays (red color) using different methods on the *In-house dataset*.

use a larger learning rate, while transformer-based methods use a smaller one. For STU-Net S, STU-Net B, STU-Net L, SwinUNETR, SwinUNETR-v2, MedNeXt, nnUNet and UMambaBot, the learning rate is set to $1e-2$, and stochastic gradient descent [3] with a momentum of 0.99 is employed as the optimizer. For TransUNet, the learning rate is set to $1e-3$, and stochastic gradient descent with a momentum of 0.99 is employed. For UNETR, the learning rate is set to $1e-5$, and the AdamW optimizer [25] is employed with betas of (0.9, 0.999).

We evaluate the segmentation performance using the Dice similarity coefficient, DSC (%), and calculate the average surface distance (ASD, *mm*) and the 95th percentile of the Hausdorff distance (HD95, *mm*) across all cases. A better-performing method should produce a higher DSC score and lower ASD and HD95 values.

4.4 Comparing to State-of-the-art Methods

In-house dataset performance. To validate the NPC GTV segmentation performance in non-contrast pCT images, we conduct a comparative analysis of our SATS against other leading segmentation methods using the in-house dataset. Table 1 summarizes the quantitative segmentation performance and model parameters. Under a relatively small number of parameters, the proposed SATS demonstrates an improvement over previous approaches. For example, SATS outperforms the transformer-based SwinUNETR-V2 in DSC, ASD, and HD95 by 0.81%, 2.6%, and 3.6%, respectively. Figure 4 presents the segmentation results of the top four performing methods (SATS, SwinUNETR-V2, SwinUNETR, and nnUNet) on a sample from the in-house dataset. It can be observed that our SATS method exhibits higher accuracy in boundary segmentation (e.g., the nasal septum).

Generalizability in external evaluation. The external testing results are summarized in Table 2 and Figure 6. Several conclusions can be drawn. First, the proposed SATS achieves the best performance as compared to all other leading methods in external evaluation. As illustrated in Figure 6 (presented in the violinplot format), our approach achieves the highest average value and lowest variability in external testing, demonstrating superior and consistent performance.

Table 2: Quantitative Results on NPC Tumor Segmentation Task. The experiment is denoted as $\text{In-house}_{train} \Rightarrow \text{External}_{test}$, which represents training on scans from the In-house dataset and segmenting images in the test set of the External dataset. \uparrow : Higher values are better. \downarrow : Lower values are better. The best-performing results are shown in bold while the second-best results are indicated by underlining.

Method	$\text{In-house}_{train} \Rightarrow \text{External}_{test}$		
	DSC \uparrow	ASD \downarrow	HD95 \downarrow
UMambaBot	63.08 ± 12.02	3.37 ± 2.28	9.22 ± 7.52
UNETR	62.56 ± 12.50	3.43 ± 2.44	9.27 ± 7.46
TransUNet	62.96 ± 13.49	3.46 ± 2.45	9.52 ± 8.16
SwinUNETR	62.90 ± 11.90	3.40 ± 2.26	9.11 ± 7.41
SwinUNETR-V2	63.81 ± 12.11	3.29 ± 2.31	8.90 ± 7.32
MedNeXt	<u>64.77 ± 12.05</u>	<u>3.21 ± 2.26</u>	9.01 ± 7.50
STU-Net S	63.50 ± 11.96	3.32 ± 2.29	9.07 ± 7.33
STU-Net B	63.54 ± 12.05	3.32 ± 2.30	9.14 ± 7.46
STU-Net L	63.50 ± 11.91	3.34 ± 2.20	9.09 ± 7.25
nnUNet	64.40 ± 11.82	3.22 ± 2.25	<u>8.84 ± 7.40</u>
SATS (Ours)	66.80 ± 12.02	2.84 ± 2.16	8.51 ± 7.84

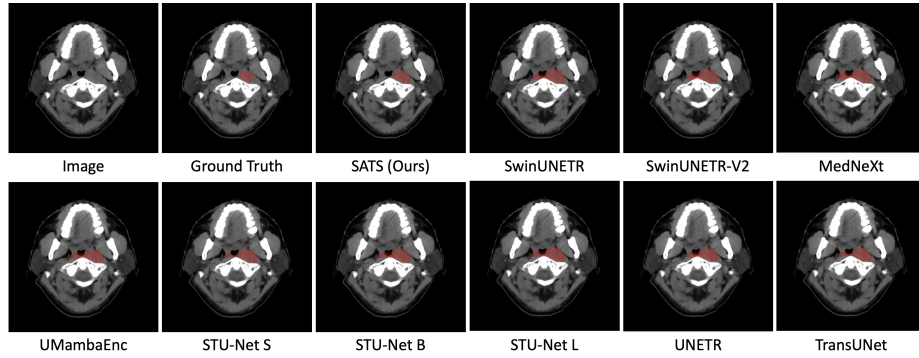


Fig. 5: Example CT slices with tumor segmentation overlays (red color) using different methods on the *External dataset*.

Second, as compared to an increase of 0.92% DSC over the 2nd best-performing method (nnUNet) in internal testing, SATS exhibits a substantial improvement of 4.4% DSC over nnUNet in external evaluation. This demonstrates the strong generalizability of the proposed semantic asymmetry learning in NPC GTV segmentation. Third, the proposed SATS consistently outperforms other leading methods in terms of ASD ($>11.8\%$ error reduction) and HD95 ($>3.7\%$ error reduction). Lastly, although SwinUNETR-V2 performs 2nd best in internal testing

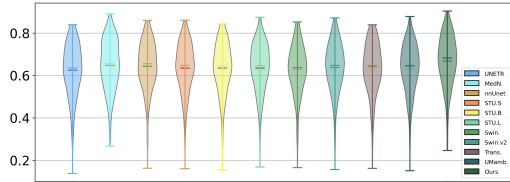


Fig. 6: Violinplots depicting the average Dice scores of gross tumors on In-house_{train} \Rightarrow External_{test} task for ten comparison methods and our method.

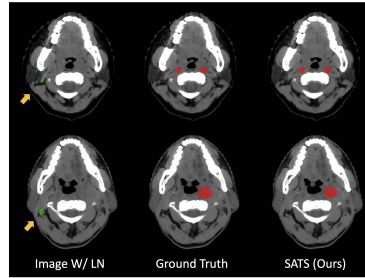


Fig. 7: Segmentation results for two nodal-involved (green) patients.

with 1.11% DSC improvement over nnUNet, nnUnet outperforms SwinUNETR-V2 in external testing by 0.61% DSC. This result indicates the strong performance of CNN-based nnUNet over transformer-based segmentation models. It is essential to highlight that our methodology reveals statistically significant differences in external validation results compared to all alternative approaches, with a two-sided p-value of less than 0.05 indicating a statistically significant difference.

Method robustness. Large primary tumors can lead to asymmetrical alterations in anatomical structures. Additionally, patients diagnosed with head and neck cancer frequently exhibit lymphatic involvement, which can substantially compromise the integrity and symmetry of surrounding anatomical features. The segmentation results illustrated in Figure 7 exemplify cases characterized by lymphatic invasion, demonstrating that our methodology exhibits robust performance in the presence of lymph nodes while effectively delineating the primary tumor.

Table 3: Influence of the effect of the projection head and margin loss on the segmentation model.

Proj. Head	Marg. Loss	DSC (%)	ASD (mm)	HD95 (mm)
\times	\times	63.44 ± 10.54	2.97 ± 1.37	7.22 ± 3.34
\times	\checkmark	61.50 ± 10.02	3.20 ± 1.39	7.73 ± 3.58
\checkmark	\checkmark	66.32 ± 10.48	2.60 ± 1.36	6.58 ± 3.50

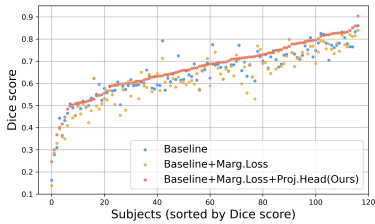


Fig. 8: Dice score compared to the baselines shown for each test subject. The Baseline represents our method without projection head and margin loss. Subjects are sorted by the Dice score of our method.

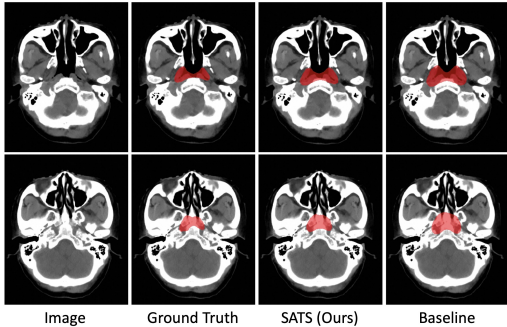


Fig. 9: Segmentation predictions for two test subjects (rows). Our method (column 3) produces more accurate segmentations than the baseline (columns 4).

4.5 Ablation Studies

Effect of projection head and margin loss on the segmentation model.

Table 3 demonstrates performance metrics for different segmentation models on the external data ($\text{In-house}_{train} \Rightarrow \text{External}_{test}$). Although the margin loss is appended, the model has lower DSC and higher ASD/HD95 than that of the initial model, suggesting that margin loss alone is insufficient to improve performance. In contrast, there is a significant performance boost (+4.98% DSC, $-0.60mm$ ASD and $-1.15mm$ HD95) when the projection head module and margin loss are appended to the baseline. Hence, the proposed semantic asymmetry learning (consisting of the projection head and margin loss) effectively improves NPC GTV segmentation accuracy.

Effect of semantic asymmetry learning. In Figures 8 and 9, we present a comparative analysis of our proposed method against the baseline configurations that exclude the projection head module and/or employ margin loss baselines. As depicted in Figure 8, our methodology achieves the highest Dice score, demonstrating consistent superiority over all baseline models across the majority of the 117 test scans. Furthermore, Figure 9 provides visualizations of the segmentation results for both the baseline approaches and our proposed method, facilitating a clearer understanding of the performance differences.

5 Conclusion

We propose a novel semantic asymmetry learning method designed to leverage the inherent asymmetrical properties of tumors in the nasopharyngeal region, thereby enhancing the accuracy of nasopharyngeal carcinoma (NPC) gross tumor volume (GTV) segmentation. Our approach employs a Siamese segmentation network with a shared encoder-decoder architecture, which simultaneously

processes original and flipped CT images. This is followed by a non-linear projection module and a distance metric learning component aimed at maximizing the disparity between abnormal and normal anatomical locations. Our method demonstrates a significant improvement in NPC GTV segmentation by effectively utilizing semantic symmetry inherent in anatomical structures, achieving superior performance compared to the state-of-the-art methods, as validated on both an internal test set and an independent external dataset. It can be potentially used in radiotherapy practice to standardize the NPC GTV delineation and reduce the workload and variation of radiation oncologists.

References

1. Bai, X., Bai, F., Huo, X., Ge, J., Mok, T.C.W., Li, Z., Xu, M., Zhou, J., Lu, L., Jin, D., Ye, X., Lu, J., Yan, K.: Matching in the wild: Learning anatomical embeddings for multi-modality images. *CoRR abs/2307.03535* (2023) 7
2. Bai, X., Hu, Y., Gong, G., Yin, Y., Xia, Y.: A deep learning approach to segmentation of nasopharyngeal carcinoma using computed tomography. *Biomedical Signal Processing and Control* **64**, 102246 (2021) 2
3. Bottou, L.: Large-scale machine learning with stochastic gradient descent. In: *Proceedings of COMPSTAT'2010: 19th International Conference on Computational Statistics Paris France, August 22-27, 2010 Keynote, Invited and Contributed Papers*. pp. 177–186. Springer (2010) 8, 9
4. Chen, H., Wang, Y., Zheng, K., Li, W., Chang, C., Harrison, A.P., Xiao, J., Hager, G.D., Lu, L., Liao, C., Miao, S.: Anatomy-aware siamese network: Exploiting semantic asymmetry for accurate pelvic fracture detection in x-ray images. In: *ECCV*. vol. 12368, pp. 239–255 (2020) 4
5. Chen, H., Qi, Y., Yin, Y., Li, T., Liu, X., Li, X., Gong, G., Wang, L.: Mmfnet: A multi-modality MRI fusion network for segmentation of nasopharyngeal carcinoma. *Neurocomputing* **394**, 27–40 (2020) 2, 3
6. Chen, J., Mei, J., Li, X., Lu, Y., Yu, Q., Wei, Q., Luo, X., Xie, Y., Adeli, E., Wang, Y., et al.: Transunet: Rethinking the u-net architecture design for medical image segmentation through the lens of transformers. *Medical Image Analysis* p. 103280 (2024) 8
7. Chen, Y.P., Chan, A.T., Le, Q.T., Blanchard, P., Sun, Y., Ma, J.: Nasopharyngeal carcinoma. *The Lancet* **394**(10192), 64–80 (2019) 2
8. Chua, M.L., Wee, J.T., Hui, E.P., Chan, A.T.: Nasopharyngeal carcinoma. *The Lancet* **387**(10022), 1012–1024 (2016) 2
9. Hatamizadeh, A., Nath, V., Tang, Y., Yang, D., Roth, H.R., Xu, D.: Swin UNETR: swin transformers for semantic segmentation of brain tumors in MRI images. In: *Brainlesion: Glioma, Multiple Sclerosis, Stroke and Traumatic Brain Injuries - 7th International Workshop, BrainLes 2021, Held in Conjunction with MICCAI 2021*. vol. 12962, pp. 272–284. Springer (2021) 8
10. Hatamizadeh, A., Tang, Y., Nath, V., Yang, D., Myronenko, A., Landman, B.A., Roth, H.R., Xu, D.: UNETR: transformers for 3d medical image segmentation. In: *IEEE/CVF Winter Conference on Applications of Computer Vision, WACV*. pp. 1748–1758. IEEE (2022) 8
11. He, Y., Nath, V., Yang, D., Tang, Y., Myronenko, A., Xu, D.: Swinunetr-v2: Stronger swin transformers with stagewise convolutions for 3d medical image segmentation. In: *Medical Image Computing and Computer Assisted Intervention - MICCAI*. vol. 14223, pp. 416–426. Springer (2023) 8

12. Heinrich, M.P., Jenkinson, M., Brady, S.M., Schnabel, J.A.: Globally optimal deformable registration on a minimum spanning tree using dense displacement sampling. In: *Medical Image Computing and Computer-Assisted Intervention*. pp. 115–122. Springer (2012) [7](#)
13. Huang, J.b., Zhuo, E., Li, H., Liu, L., Cai, H., Ou, Y.: Achieving accurate segmentation of nasopharyngeal carcinoma in mr images through recurrent attention. In: *Medical Image Computing and Computer Assisted Intervention–MICCAI 2019: 22nd International Conference, Shenzhen, China, October 13–17, 2019, Proceedings, Part V 22*. pp. 494–502. Springer (2019) [2](#)
14. Huang, J., Li, H., Li, G., Wan, X.: Attentive symmetric autoencoder for brain MRI segmentation. In: *Medical Image Computing and Computer Assisted Intervention - MICCAI. Lecture Notes in Computer Science*, vol. 13435, pp. 203–213. Springer (2022) [4](#)
15. Huang, Z., Wang, H., Deng, Z., Ye, J., Su, Y., Sun, H., He, J., Gu, Y., Gu, L., Zhang, S., Qiao, Y.: Stu-net: Scalable and transferable medical image segmentation models empowered by large-scale supervised pre-training. *CoRR* **abs/2304.06716** (2023) [8](#)
16. Isensee, F., Wald, T., Ulrich, C., Baumgartner, M., Roy, S., Maier-Hein, K., Jaeger, P.F.: nnu-net revisited: A call for rigorous validation in 3d medical image segmentation. In: *International Conference on Medical Image Computing and Computer-Assisted Intervention*. pp. 488–498. Springer (2024) [8](#)
17. Ke, L., Deng, Y., Xia, W., Qiang, M., Chen, X., Liu, K., Jing, B., He, C., Xie, C., Guo, X., et al.: Development of a self-constrained 3d densenet model in automatic detection and segmentation of nasopharyngeal carcinoma using magnetic resonance images. *Oral Oncology* **110**, 104862 (2020) [2](#)
18. Lee, A.W., Ng, W.T., Pan, J.J., Poh, S.S., Ahn, Y.C., AlHussain, H., Corry, J., Grau, C., Grégoire, V., Harrington, K.J., et al.: International guideline for the delineation of the clinical target volumes (ctv) for nasopharyngeal carcinoma. *Radiotherapy and Oncology* **126**(1), 25–36 (2018) [7](#)
19. Li, S., Xiao, J., He, L., Peng, X., Yuan, X.: The tumor target segmentation of nasopharyngeal cancer in ct images based on deep learning methods. *Technology in cancer research & treatment* **18**, 153–160 (2019) [2](#)
20. Li, Y., Dan, T., Li, H., Chen, J., Peng, H., Liu, L., Cai, H.: Npcnet: Jointly segment primary nasopharyngeal carcinoma tumors and metastatic lymph nodes in mr images. *IEEE Transactions on Medical Imaging* **41**(7), 1639–1650 (2022) [2](#), [3](#)
21. Liao, W., He, J., Luo, X., Wu, M., Shen, Y., Li, C., Xiao, J., Wang, G., Chen, N.: Automatic delineation of gross tumor volume based on magnetic resonance imaging by performing a novel semisupervised learning framework in nasopharyngeal carcinoma. *International Journal of Radiation Oncology* Biology* Physics* **113**(4), 893–902 (2022) [2](#)
22. Lin, L., Dou, Q., Jin, Y.M., Zhou, G.Q., Tang, Y.Q., Chen, W.L., Su, B.A., Liu, F., Tao, C.J., Jiang, N., et al.: Deep learning for automated contouring of primary tumor volumes by mri for nasopharyngeal carcinoma. *Radiology* **291**(3), 677–686 (2019) [2](#)
23. Liu, C.F., Padhy, S., Ramachandran, S., Wang, V.X., Efimov, A., Bernal, A., Shi, L., Vaillant, M., Ratnanather, J.T., Faria, A.V., et al.: Using deep siamese neural networks for detection of brain asymmetries associated with alzheimer’s disease and mild cognitive impairment. *Magnetic resonance imaging* **64**, 190–199 (2019) [4](#)
24. Liu, Y., Zhou, Z., Zhang, S., Luo, L., Zhang, Q., Zhang, F., Li, X., Wang, Y., Yu, Y.: From unilateral to bilateral learning: Detecting mammogram masses with

- contrasted bilateral network. In: *Medical Image Computing and Computer Assisted Intervention - MICCAI*. vol. 11769, pp. 477–485. Springer (2019) [4](#)
25. Loshchilov, I., Hutter, F.: Decoupled weight decay regularization. In: *7th International Conference on Learning Representations, ICLR 2019, New Orleans, LA, USA, May 6-9, 2019*. OpenReview.net (2019) [9](#)
 26. Luo, X., Fu, J., Zhong, Y., Liu, S., Han, B., Astaraki, M., Bendazzoli, S., Tomadasu, I., Ye, Y., Chen, Z., et al.: Segrap2023: A benchmark of organs-at-risk and gross tumor volume segmentation for radiotherapy planning of nasopharyngeal carcinoma. *arXiv preprint arXiv:2312.09576* (2023) [3](#)
 27. Luo, X., Liao, W., Chen, J., Song, T., Chen, Y., Zhang, S., Chen, N., Wang, G., Zhang, S.: Efficient semi-supervised gross target volume of nasopharyngeal carcinoma segmentation via uncertainty rectified pyramid consistency. In: *Medical Image Computing and Computer Assisted Intervention–MICCAI 2021: 24th International Conference, Strasbourg, France, September 27–October 1, 2021, Proceedings, Part II* 24. pp. 318–329. Springer (2021) [2](#)
 28. Luo, X., Liao, W., He, Y., Tang, F., Wu, M., Shen, Y., Huang, H., Song, T., Li, K., Zhang, S., et al.: Deep learning-based accurate delineation of primary gross tumor volume of nasopharyngeal carcinoma on heterogeneous magnetic resonance imaging: a large-scale and multi-center study. *Radiotherapy and Oncology* p. 109480 (2023) [2](#)
 29. Ma, J., Li, F., Wang, B.: U-mamba: Enhancing long-range dependency for biomedical image segmentation. *CoRR* **abs/2401.04722** (2024) [8](#)
 30. Ma, Z., Zhou, S., Wu, X., Zhang, H., Yan, W., Sun, S., Zhou, J.: Nasopharyngeal carcinoma segmentation based on enhanced convolutional neural networks using multi-modal metric learning. *Physics in Medicine & Biology* **64**(2), 025005 (2019) [2](#)
 31. Mei, H., Lei, W., Gu, R., Ye, S., Sun, Z., Zhang, S., Wang, G.: Automatic segmentation of gross target volume of nasopharynx cancer using ensemble of multiscale deep neural networks with spatial attention. *Neurocomputing* **438**, 211–222 (2021) [2](#)
 32. Men, K., Chen, X., Zhang, Y., Zhang, T., Dai, J., Yi, J., Li, Y.: Deep deconvolutional neural network for target segmentation of nasopharyngeal cancer in planning computed tomography images. *Frontiers in oncology* **7**, 315 (2017) [2](#), [3](#)
 33. Razek, A.A.K.A., King, A.: Mri and ct of nasopharyngeal carcinoma. *American Journal of Roentgenology* **198**(1), 11–18 (2012) [2](#)
 34. Roy, S., Köhler, G., Ulrich, C., Baumgartner, M., Petersen, J., Isensee, F., Jäger, P.F., Maier-Hein, K.H.: Mednext: Transformer-driven scaling of convnets for medical image segmentation. In: *Medical Image Computing and Computer Assisted Intervention - MICCAI*. vol. 14223, pp. 405–415. Springer (2023) [8](#)
 35. Tian, L., Li, Z., Liu, F., Bai, X., Ge, J., Lu, L., Niethammer, M., Ye, X., Yan, K., Jin, D.: Same++: A self-supervised anatomical embeddings enhanced medical image registration framework using stable sampling and regularized transformation. *ArXiv* **abs/2311.14986** (2023) [5](#)
 36. Wang, H., Chen, J., Zhang, S., He, Y., Xu, J., Wu, M., He, J., Liao, W., Luo, X.: Dual-reference source-free active domain adaptation for nasopharyngeal carcinoma tumor segmentation across multiple hospitals. *CoRR* **abs/2309.13401** (2023) [3](#)